Journal of Alloys and Compounds 776 (2019) 475–485

Contents lists available at ScienceDirect

Journal of Alloys and Compounds

journal homepage: http://www.elsevier.com/locate/jalcom

The influence of synthesis conditions on the redox behaviour of $LiFePO_4$ in aqueous solution

Radovan Georgijević [a], Milica Vujković [a, *], Sanjin Gutić [b], Meho Aliefendić [b], Dragana Jugović [c], Miodrag Mitrić [d], Veljko Đokić [e], Slavko Mentus [a, f]

[a] Faculty of Physical Chemistry, University of Belgrade, Studentski trg 12-16, 11158 Belgrade, Serbia
[b] University of Sarajevo, Faculty of Science, Department of Chemistry, Zmaja od Bosne 33-35, Sarajevo, Bosnia and Herzegovina
[c] Institute of Technical Sciences of SASA, Knez Mihailova 35/IV, 11 000 Belgrade, Serbia
[d] Institute of Nuclear Sciences "Vinča", Mike Petrovića Alasa 12-14, 11001 Belgrade, University of Belgrade, Serbia
[e] Faculty of Technology and Metallurgy, University of Belgrade, Karnegijeva 4, 11000 Belgrade, Serbia
[f] Serbian Academy of Sciences and Arts, Knez Mihajlova 35, 11000 Belgrade, Serbia

ARTICLE INFO

Article history:
Received 21 July 2018
Received in revised form
30 September 2018
Accepted 20 October 2018
Available online 24 October 2018

Keywords:
Olivine $LiFePO_4$
Aqueous electrolyte
Kinetics of lithium redox behaviour

ABSTRACT

To contribute to the knowledge on the influence of synthesis procedure on the intercalation kinetics of lithium ions into phospho-olivines, $LiFePO_4$/C composite samples (LFPC) were synthesized in two ways, the first one in a sol-gel procedure (SG), and the other in a solid-state reaction (SS). The X-ray diffractograms (XRD) of both samples overlapped with that of pure $LiFePO_4$, taken from the crystallographic database. Scanning electron microscopy pictures indicated the high degree of interparticle sintering, which caused a considerable agglomerate growth. The results of potentiodynamic measurements in aqueous $LiNO_3$ solution revealed that for SS sample, three times higher initial capacity from that of SG one, (amounting to 74 mAh g^{-1} at 5 mV s^{-1}). However, capacity fade on rising scan rate is much more expressed for SS sample than for SG one. We suggest that a different degree of material utilization due to the incomplete coverage of olivine particles by carbon explains this difference. The technique of separation of diffusion and capacitance currents was applied in a kinetic analysis, but it was shown to be inappropriate. We suggest the inapplicability of classic CV theory to the intercalation system accompanied by phase transition. Instead, a model of ohmic resistance determination of process kinetics was considered. LFPC-SS sample delivers three times larger capacity in $LiNO_3$, amounting to 74 mAh g^{-1} at 1 mV s^{-1}.

1. Introduction

Since the olivine $LiFePO_4$ was introduced into the intercalation electrochemistry by Goodenough et al. [1], numerous studies were devoted to achieve its high theoretical coulombic capacity of 170 mAh g^{-1}. However, slow lithium diffusion and low electronic conductivity, together with the property of olivine known as "anti-site" defects [2–4], seemed to be insurmountable barriers in early studies [5]. Today, these obstacles are surmounted for organic electrolytes. The capacity close to the theoretical one, depending only slightly on charging/discharging rates was achieved, which enabled a commercial use of the $LiFePO_4$ olivine [6–8].

Manickam et al. [9] reported the ability of $LiFePO_4$ to intercalate reversibly Li^+ ions in aqueous electrolyte solutions. After many studies by different authors [10–16] the possibility was discovered that $LiFePO_4$ may serve as the cathode material of aqueous rechargeable lithium-ion batteries (ARLB). A direct reaction of olivine phase with aqueous electrolyte solution was found to cause pronounced capacity fade [15]. Also, the capacity of olivine may decrease significantly on the increase of the charging/discharging rate. A deeper understanding of redox chemistry of $LiFePO_4$ in aqueous solutions might be helpful in removing of these shortcomings.

Charge storage based on lithium-ion intercalation is preferably bulk process, requiring diffusion through solid bulk, which may be easily a slow step in the intercalation redox kinetics, especially at higher charging/discharging rates. During intercalation, a part of Li^+ ions may be captured by surface sites, contributing to the

* Corresponding author.
E-mail address: milica.vujkovic@ffh.bg.ac.rs (M. Vujković).

https://doi.org/10.1016/j.jallcom.2018.10.246
0925-8388/

pseudocapacitance, which is commensurate to the specific surface area [17,18]. The capacity caused by surface processes is not too sensitive to charging/discharging rate, thus the participation of pseudocapacity rises with the rise in the charging/discharging rate. By reducing the particle size to nanoscale the ratio of surface area to volume increases providing a higher rate capability [19–21]. Although the intercalation pseudocapacitance is usually associated with the surface processes, it could also originate from the bulk storage of Li^+ ions [22]. This requires a very fast diffusion of intercalated ions.

Recently, a high rate capability based on either Li^+ or Na^+ intercalation pseudocapacitance has been observed in various intercalation materials [22–32]. A high fraction of pseudocapacitance in total coulombic capacitance was mostly observed in layered crystal nanostructures with open channels such as T-Nb_2O_5 [22–24,33], VS_2 [27], TiS_2 and MoS_2 [29,30], V-, Mo- and Ti-based oxides [25,26,31,34,35], but this type of charge storage is not typical for materials displaying phase transition induced by intercalation reaction (e.g., $LiFePO_4$ and $Li_4Ti_5O_{12}$). A high fraction of pseudocapacitance was found during sodiation of $LiFePO_4$ and $Li_4Ti_5O_{12}$ [36,37].

Lithium intercalation/deintercalation process of $LiFePO_4$, accompanied by reversible phase transition $LiFePO_4 \leftrightarrow FePO_4$ transition at ~3.5 V vs. Li^+/Li, displays diffusion control [17,38]. Wang et al. [39] suggested that the fraction of the total charge of $LiFePO_4$ lithiation, consumed before the galvanostatic curve undergoes a step change, is not due to the single-phase diffusion-controlled process, but from the pseudocapacitance. In this potential region, Fe^{3+} defect sites in the amorphous $LiFePO_4$ which surrounds crystalline olivine $LiFePO_4$ phase may also contribute to the pseudocapacitance [7].

In order to determine separated contributions of bulk and surface charge in total charge stored in an intercalation process, the Dunn's group [22,40,41] proposed a method, based on the power law, which is widely accepted in the scientific community [20–25,42-44].

In this study, we synthesized $LiFePO_4$/C composites avoiding methods which provide highest coulombic capacity [10,11], but using methods providing tinny crystals ratios of crystalline versus amorphous phase. Adopting the method proposed by Dunn et al. [22,40,41], we performed a detailed kinetic analysis of intercalation/deintercalation reactions in an aqueous solution of lithium salts. The goal was to estimate which of two synthesis procedures provides better electrode material, and why. The kinetic analysis of $LiFePO_4$, by means of cyclic voltammetry, has already been performed in organic electrolytes [38,45–47], but rarely in aqueous electrolytes [48]. Thus, the use of aqueous electrolyte may be treated as a second particularity of this study.

2. Experimental

2.1. Sample synthesis

The $LiFePO_4$/C composite was synthesized in two ways, by sol-gel method and solid-state reaction, according to the scheme presented in Fig. 1. In the sol-gel synthesis procedure, oxalic acid was used as a complexing and reducing agent, and sucrose as a carbon source. The use of oxalic acid enabled easy formation of transparent sol without the need to control pH [49]. In the solid-state reaction procedure, stearic acid was used as a carbon source and a reducing agent.

2.1.1. Sol-gel synthesis route

50 ml of aqueous solution containing 14.84 g $FeSO_4x7H_2O$ was mixed with the 20 ml aqueous solution containing 4.09 g $NH_4H_2PO_4$. A solution of NH_3xH_2O was added in this mixture to pH value 9. The resulting mixture was stirred with a magnetic stirrer for 30 min at room temperature, whereby $Fe_3(PO_4)_2 \times 8H_2O$ precipitated, according to the equation:

$$3Fe^{2+} + 2PO_4^{3-} + 8H_2O \rightarrow Fe_3(PO_4)_2 \times 8H_2O \quad (1)$$

The precipitate was filtered, rinsed with distilled water and transferred into a 2 M solution of H_3PO_4. After addition of 2.73 ml H_2O_2 (10 M) to the obtained solution, both oxalic acid, LiOH and sucrose were added to the mixture, in an amount providing 10% by weight of carbon content in the final product. LiOH was also added to the mixture, in a stoichiometric amount relative to ferrous sulphate and ammonium phosphate. The resulting sol was dried overnight in an air atmosphere at 90 °C, afterwards, xerogel was obtained. Xerogel was annealed first at 350 °C and then at 700 °C under a nitrogen atmosphere with an intermittent introduction of hydrogen. The resulting powder was labelled as SG.

2.1.2. The solid-state reaction procedure

For this procedure, iron(III)phosphate ($FePO_4$), served as a precursor. The first steps of its preparation do not differ from the above described sol-gel synthesis before addition of oxalic acid, sucrose and LiOH. In continuation, after the oxidation of Fe(II) to Fe(III) by hydrogen peroxide, a solution of NH_3 xH_2O was added to pH value 9. The obtained emulsion was stirred for 6 h at 90 °C, until the pale yellow precipitate $FePO_4x2H_2O$ was formed.

$$2Fe_3(PO_4)_2 \times 8H_2O + 6H^+ + 2PO_4^{3-} + 3H_2O_2 \rightarrow 6FePO_4x2H_2O + 12H_2O \quad (2)$$

This precipitate was dried at 120 °C for 5 h, and then at 500 °C for 6 h, to obtain the final form of $FePO_4$ precursor powder.

1.542 g LiOH was powdered in a mortar and mixed with a solution of 2.7 g stearic acid, in 25 mL of isopropanol. The resulting mixture was mixed in a mortar under gradual addition of 50 mL of isopropanol. Subsequently, 8,8290 g $FePO_4$ precursor and an additional amount of 5 mL (i.e. 55 ml in total) of isopropanol were added, and the suspension was homogenized by stirring. Isopropanol was removed by evaporation at 50 °C under permanent stirring by a magnetic stirrer. The resulting solid reaction mixture was thermally treated under a nitrogen atmosphere, with an intermittent introduction of hydrogen. The temperature was gradually raised to 710 °C for 30 min, and the annealing is continued at a preset temperature for 6 h. The product, $LiFePO_4$/C composite (SS), was cooled spontaneously to ambient temperature.

2.2. Preparation of the working electrode

For cyclic voltammetry (CV) investigations, glassy carbon disk was used as a support of electrode material. For this purpose, the electrode material was mixed with nanostructured carbon (Vulcan CX 72) and polyvinylidene fluoride (PVDF), in a weight ratio of 75:20:5, respectively. Nanostructured carbon served as the conductivity supporting additive, while PVDF was the binder. By adding N-methyl-2-pyrrolidone, a suspension was formed. After 60 min of homogenization in an ultrasonic bath, a droplet of the suspension was spread uniformly over the glassy carbon surface, and the solvent was evaporated by heating first at 60 °C in air, and then at 130 °C in vacuum for 4 h.

2.3. Experimental methods

For the characterization of the synthesized materials, the following methods were used: X-ray diffraction (XRD), scanning

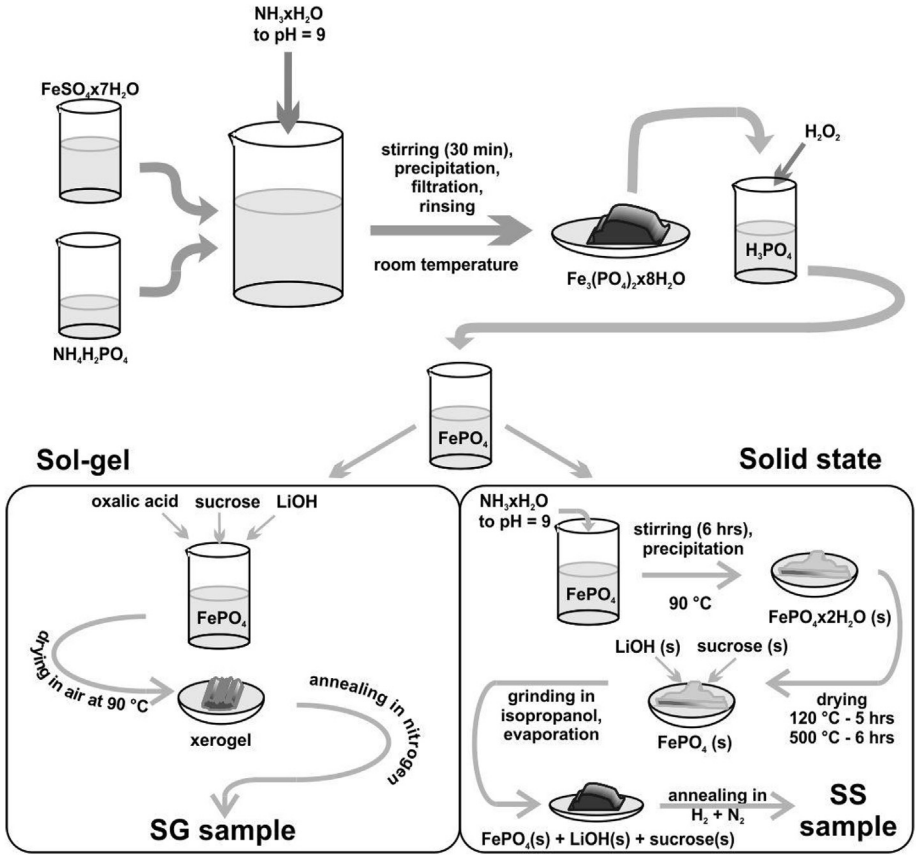

Fig. 1. Schematic illustration of the synthesis processes.

electron microscopy, thermal analysis and cyclic voltammetry.

The phase composition was determined by room temperature X-ray powder diffractometry using Philips PW 1050 diffractometer and Ni-filtered $CuK_{\alpha 1,2}$ radiation with the wavelength $\lambda_{1,2} = 1.5418$ Å, in the 2θ range 10–70° at 0.05° increments and an exposure time of 3 s per step.

The morphology of samples was observed by scanning electron microscopy (SEM) using JEOL JSM 7001F microscope.

The textural parameters of the samples were measured using an accelerated surface area and porosity system- ASAP 2020. The samples were previously degassed under vacuum at 105 °C for 10 h.

Simultaneous TG-DTA thermal analysis was carried out by means of the TA SDT 2960 instruments, which served to determine the carbon content in the composite samples. The measurement was conducted under an air atmosphere with the heating rate of 10 °C min^{-1}.

Cyclic voltammetry (CV) measurements were carried out by Gamry PCI4/300 Potentiostat/Galvanostat/ZRA, in a three electrode cell open to the air, filled by 6 M $LiNO_3$ aqueous solution. The potentials were measured relative to SCE within the water stability interval. A platinum foil was used as a counter electrode.

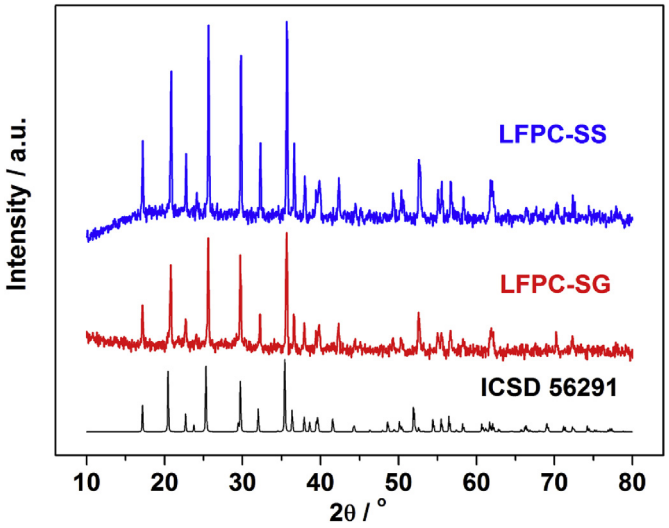

Fig. 2. X-ray diffraction patterns of the composites LFPC obtained by -SS and -SG over the reference diffractogram ICSD 56291.

3. Results and discussion

3.1. X-ray diffractometry and scanning electron microscopy characterization of samples

The crystal structure of the as-synthesized powdery SG and SS samples was confirmed by X-ray powder diffraction (Fig. 2). The diffraction lines overlap exactly with the reflections of the diffraction patterns of $LiFePO_4$ taken from a crystallographic database ICSD, Card No. 56291. This indicates that olivine structure $LiFePO_4$ was successfully obtained by both synthesis methods. The diffractograms do not reveal the presence of carbon, as a consequence of its low crystal ordering, however, its presence was evidenced and determined by thermogravimetry (Table 1).

Lattice parameters were determined by using the Le Bail's whole

Table 1
Lattice parameters, mean coherent domain size, carbon content, and X-ray crystallinity of the synthesized powders.

	a [Å]	*b* [Å]	*c* [Å]	Mean coherent domain size [nm]	Carbon content [wt%]	X-ray crystallinity [%]
LFPC-SS	10.3316	6.0069	4.6925	331	5	94
LFPC-SG	10.3293	6.0085	4.6920	203	14	74

profile unit cell refinement [50] within the FullProf program and the obtained values are given in Table 1. In addition, the coherent domain sizes, given in Table 1, were calculated by using X-ray Line Profile Fitting Program (XFIT) with a Fundamental Parameters convolution approach to generating line profiles [51]. Principally, Scherrer formula enables a rough estimation of crystallite size (from the FWHM), since the broadening of the reflection is not only due to the domain size, but is also due to the microstrain and instrumental line broadening. For the determination of coherently scattering domain size, i.e. crystallite size, instead of the Scherrer method, we used more precise one which takes into account both instrumental line broadening and microstrain.

It appears that the powder obtained by sol-gel synthesis has a smaller mean coherent domain size, decreased *a* lattice parameter and increased lattice parameter *b*. A deconvolution of the intensity profile curves into an amorphous halo and several discrete crystalline diffraction peaks can be used for an estimation of X-ray crystallinity. The X-ray crystallinity of the sample is equal to the ratio of the area of crystalline fraction and the sum of areas of crystalline and amorphous fractions. The amorphous halo of the sample obtained by sol-gel synthesis is greater than the calculated carbon content. This can be interpreted as there is an additional phase in the sample, which is either in an amorphous or highly distorted state, considering that crystal lattice distortions cannot be properly distinguished from the amorphous halo.

The SEM pictures of both SG and SS samples are shown in Fig. 3. Both composites have a quite heterogeneous morphology, which is made up of irregularly shaped particles initially 0.1 μm in size, grouped by sintering into agglomerates with the dimensions in the 1–10 μm range (Fig. 3a,c). Due to the partial melting, some particles of SG sample look like solidified spherical droplets. The gradual growth of different particles incorporated into SG agglomerates, up to several microns in size, can be observed in Fig.3a too. The assembles of particles different in size make the surface of SG particles rather rough, revealing voluminous inter-particle space (formed as a consequence of liberation of gas bubbles during the synthesis), while micron- and submicron-sized SS agglomerates look pretty smooth.

Compared to the formerly published synthesis with vanadium additive, where particle size remained in the nanometer range [10], one may conclude that in the here applied synthesis procedures much higher degree of agglomeration by sintering was achieved, as a consequence of long heating at 710 °C.

The particle growth which occurs along with the sintering, as obvious from the SEM pictures, is advantageous for crystal phase purity, however, it may be disadvantageous with respect to uniform coverage by carbon. Namely, partial melting of sample particles during sintering, evidenced by the appearance of solidified droplets, led to carbon redistribution into mutually insulated agglomerates, which consequently may lead to an incomplete utilization of $LiFePO_4$ during charging/discharging processes. The carbon crowding is more visible in the pictures of the SG sample, which according to TG analysis contains almost three times higher amount of carbon relative to the SS sample.

3.2. BET measurements of specific surface area

The specific surface areas of samples, measured by BET method,

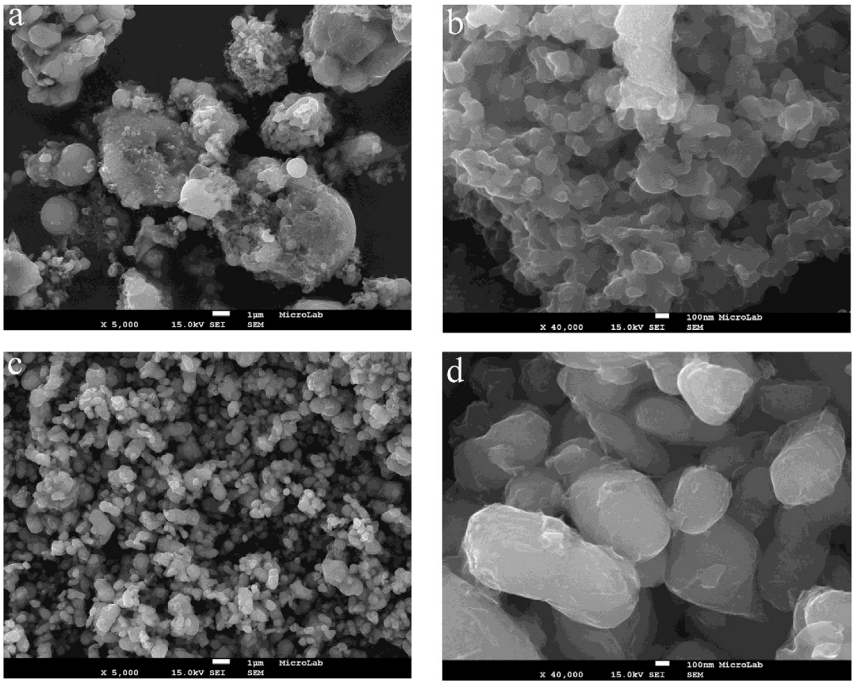

Fig. 3. Representative SEM figure of SG (a,b) and SS (c,d) samples.

were found to be 16.3 m^2/g (SG) and 4.68 m^2/g (SS). The difference in the specific surface area originates from the difference in the fraction of carbon wrapping olivine particles. The porosity type of carbon layer may control the utilization of olivine, since the pores act as transporting channels for ions participating in the intercalation. Actually, mean mesopore diameter, D_{mean} (nm) was found to be 11.6 nm (for SG) and 21.05 nm (for SS). Therefore, under a common current regime, the porosity of the SS sample, enables more facile transport of Li^+ ions.

3.3. Thermogravimetric analysis

In Fig. 4, TG/DTA diagrams of both SG (a) and SS samples (b), measured in an air atmosphere, in the temperature range from ambient temperature up to 750 °C, are presented. The thermogravimetric determination of the carbon content in $LiFePO_4$/C composites by heating in air flow, is aggravated by oxidation of iron (which causes mass increase) that occurs almost simultaneously to the mass loss caused by carbon combustion [11,52].

The oxidation of olivine [52], consisting in the oxidation of Fe^{2+} ions to Fe^{3+}, proceeds according to the reaction $LiFePO_4 + 1/4O_2 \rightarrow 1/3\ Li_3Fe_2(PO_4)_3 + 1/6\ Fe_2O_3$, causing a mass increase for 5.07%. That occurs between 400° and 600° C. Since simultaneously carbon combustion occurs, the TG curve is a resultant of this mass gain and mass loss. The carbon content should be determined as the difference between plateau heights at ~300 °C and ~650 °C, supplemented by 5.07%.

According to this calculation, the SG composite sample contained 14 wt% while SS sample contained 5 wt% of carbon formed in the very synthesis procedure.

3.4. Redox behaviour in an aqueous electrolytic solution

The electrochemical behaviour of SG and SS samples in an aqueous 6 M $LiNO_3$ solutions was examined by cyclic voltammetry. The obtained results are presented in Figs. 5 and 6, in a way which enables their comparison.

Typical redox peaks (0.125/0.359 V vs. SCE at 20 mV s^{-1}) corresponding to the Fe^{2+}/Fe^{3+} redox reaction accompanying both lithiation/delithiation and phase transition $LiFePO_4 \leftrightarrow FePO_4$, can be clearly seen in Fig. 5. The peaks display initial increase on cycling (not illustrated graphically), however, five cycles are sufficient to achieve a stable potentiodynamic response. The stabilization may be due to the gradual penetration of the electrolyte to the olivine particles [53,54].

After stabilization, CVs were recorded at different polarization rates in the 5–400 mV s^{-1} range (Fig. 5 a,b). The peak-to-peak distance, 118 mV ($\Delta E/2 = 56$ mV) for 5 mV s^{-1} which, if the classic theory of CV may apply, would mean a quasireversible (simultaneously electron and mass transfer controlled) redox processes. However, the fronts of peaks recorded at various scan rates look like a linear function of potential and those recorded at various scan rates have an identical slope, which is indicative of ohmic resistance control of overall process, as discussed firstly by Dahn et al. [55] and recently by Mentus et al. [56].

Cyclic voltammograms maintain their shape not only through the cycling (Fig. S1a) but also up to a very high polarization rate (Fig. 5b), indicating the ability of the SG material to undergo fast redox reactions and keep a stable coulombic capacity. There are no changes in the basic shape of redox peaks, indicating an excellent sustainability of the sample's redox activity at very high currents.

The cyclic voltammograms of SS sample recorded in aqueous 6 M $LiNO_3$ solution are shown in Fig. 6.

The shape of the cyclovoltammograms was stabilized rather quickly, indicating good wettability of the SS sample. After stabilization, the cyclic voltammograms were recorded at different polarization rates from 5 to 20 mV s^{-1} (Fig. 6a) and from 50 to 400 mV s^{-1} (Fig. 6b). Despite the relatively small carbon content in the SS sample, its cyclovoltammograms displayed high stability on cycling (Fig. S1b). The basic shape of the CV curves remained unchanged at rising scan rate, although anodic peaks slightly lost their sharpness. When after application of high polarization rate CV was recorded again at 20 mV s^{-1} (Fig. 6c), a slight current drop was registered. This indicated that the material may lose some of its activity if subjected to fast polarization, which was not observed in the case of the SG sample.

3.4.1. Comparison of coulombic capacity of SG and SS samples

The cyclic voltammograms of SG and SS samples recorded in aqueous $LiNO_3$ solution at a common scan rate (Figs. 5 and 6), indicate a clear difference in both intercalation kinetics and in coulombic capacity. The SS sample displays higher currents which are indication of faster reactions. However, it displays also remarkably larger peak-to-peak potential distance, namely (560 mV versus ~ 284 mV for SG), which may be an indication of slower electron transfer reactions in SS case, if the classical theory of CV might be valid in this case.

Independently on the applicability of the classic CV theory in the kinetic investigations, the surface encompassed by the CV curve is doubtless a reliable measure of the number of coulombs consumed on deintercalation (anodic part of CV), and intercalation (cathodic part of CV) processes. Thus, the integration of cathodic and anodic part of the CV curve is a tool to determine coulombic capacity. In this way, we determined the capacities of the investigated samples at various scan rates and displayed it in Fig. 7.

The SS sample displays three times larger initial lithium storage

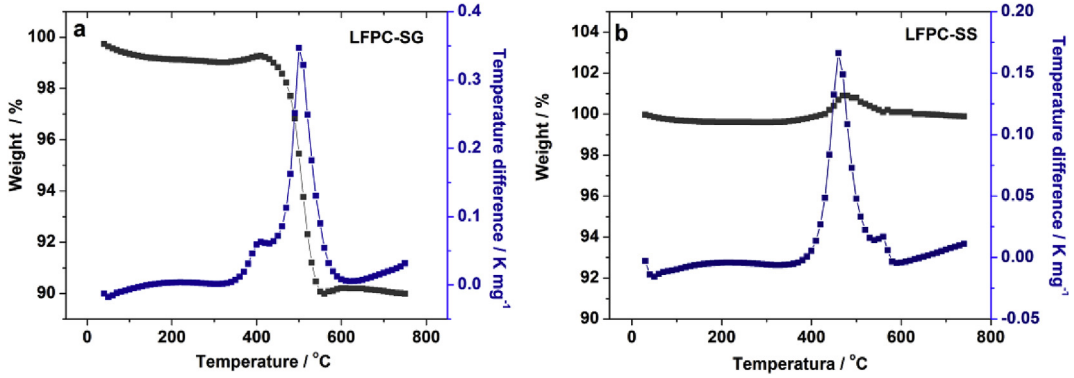

Fig. 4. The TG/DTA curves of the SG (a) and SS (b) samples under an air flow at a heating rate 10°/C.

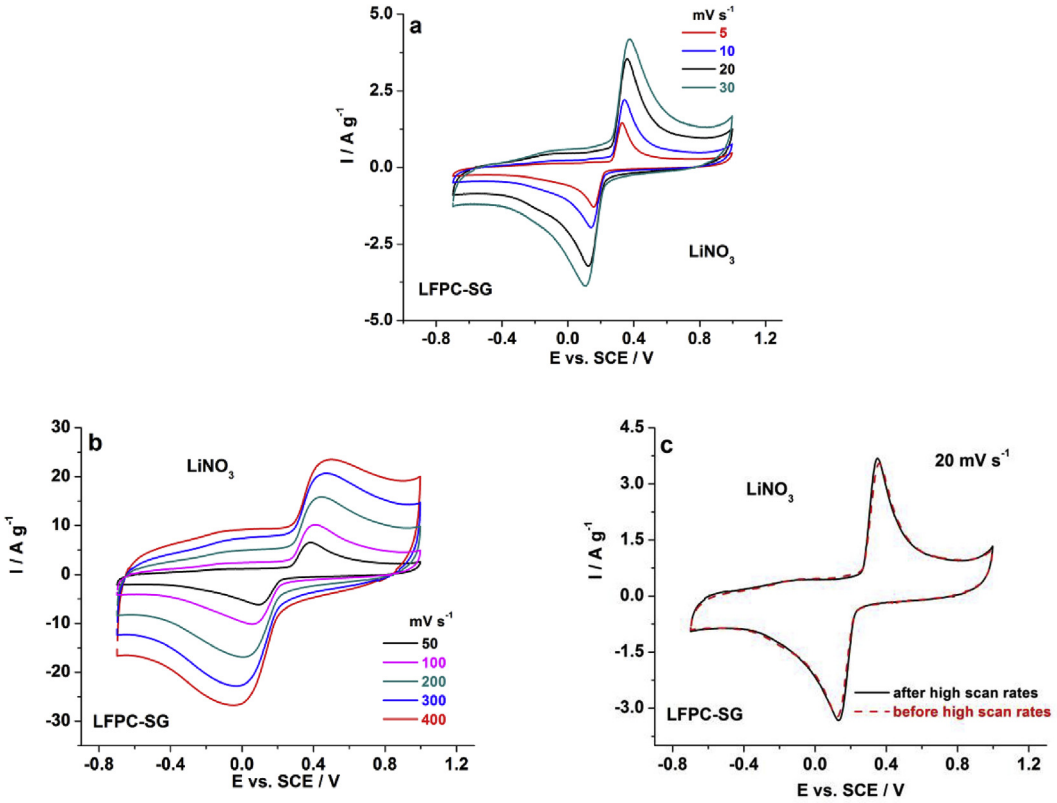

Fig. 5. Cyclic voltammograms of SG sample in aqueous 6 M $LiNO_3$ solution at different scan rates from a) 5 to50 and b) 50 to 400 mVs^{-1}; c) the two cyclovoltammograms recorded at 20 $mV\,s^{-1}$ with one intermediate cycle (not shown) at 400 mVs^{-1} to illustrate shape stability.

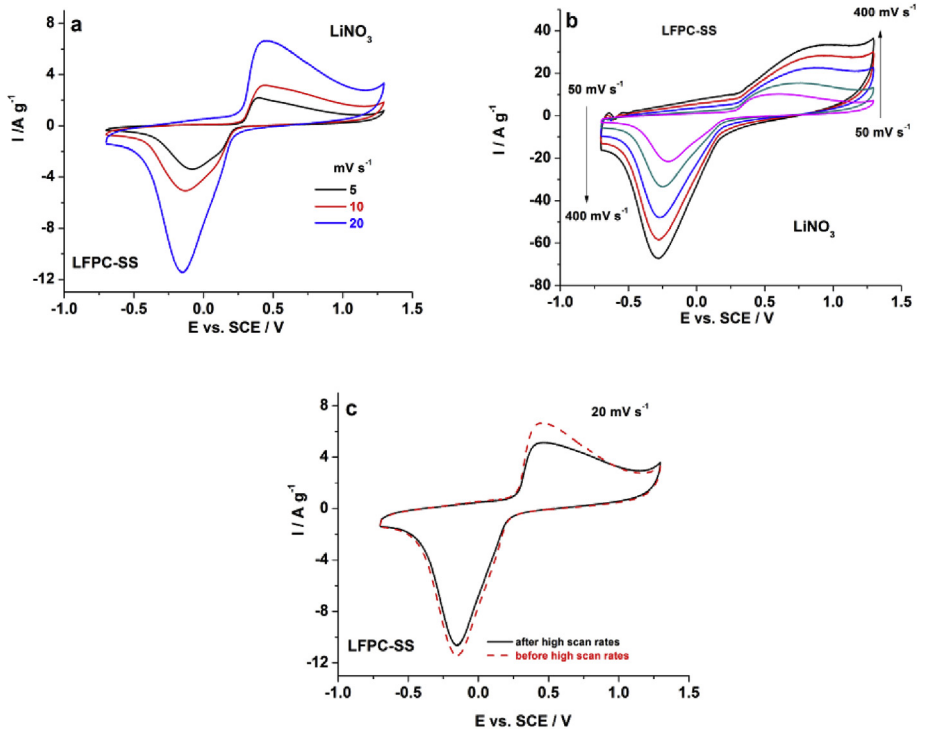

Fig. 6. Cyclic voltammograms of LFPC-SS sample in aqueous 6 M $LiNO_3$ solution at: a) low polarization rates, b) high polarization rates; c) two cycles at 20 $mV\,s^{-1}$ with one intermediate cycle (not shown) at 400 $mV\,s^{-1}$.

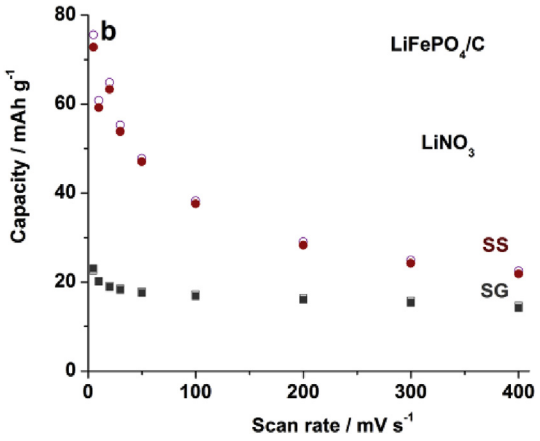

Fig. 7. Comparison of the specific capacities of SS and SG samples in aqueous 6 M $LiNO_3$ solution calculated from the voltammogram surfaces; the solid symbols relate to the intercalation and the empty symbols relate to the deintercalation.

capacity (Fig. 7) compared to SG one. Namely, initial specific capacity, at a polarization rate of 5 mV s^{-1}, amounted to ~74 mAh g^{-1} for SS sample, while the corresponding value for SG sample was only 23 mAh g^{-1}.

One can note that there are two key particularities in the capacitive performances of the examined samples. Namely, i) initial capacity is significantly higher, and ii) capacity fade accompanying the increase in scan rate is significantly faster for SS sample compared to SG one. Both capacities are lower than theoretical one (~170 mAh g^{-1}). To explain this, one may recall that pure olivine is one of the slowest intercalation electrode materials, and it may be completely utilized only at very slow current rates of the order 1 μV s^{-1}. On the other hand, CV is a fast method, and even the lowest applied scan rate of 5 mV s^{-1} may be too high to utilize the electrode material completely. As described in many of published papers [53,54], the degree of utilization may achieve unit at high intercalation rates by reducing particle size and by covering them by an electronic conductor, such as carbon shell is. From these aspects, we may comment the diagrams in Fig. 7 as follows: The way of synthesis of both SS and SG sample enabled to obtain relatively huge agglomerates of particles grown by sintering, only partially wrapped by carbon shell. Thus, only the agglomerate fraction covered by carbon undergoes charging/discharging processes enough fast to be detected by cyclic voltammetry in the used scan rate range 5–400 mV s^{-1}. This means that the utilization of the electrode material is incomplete in the used range of scan rates. The degree of coverage by carbon, in spite of its higher total percentage, is effectively somewhat lower in the SG sample. This is why scanning rates ranging from 5 to 400 mV s^{-1} belong to the region in which the degree of utilization of electrode material tapered off to its minimum, where the dependence on the scan rate becomes negligible.

3.5. Check of the ways to determine the contribution of diffusion and capacitance current in the total charge storage

The following equations were widely explored to distinguish between diffusion and capacitance current in the CV and estimate their relative participation in dependence on the scan rate [22,33,40,41,57–60].

The equation

$$Ip = av^b \quad (3)$$

where a and b are constants, is generally valid. For reversible electrode processes, the criterion $b = 0.5$ means a completely diffusion controlled process and while $b = 1$ is an indication a completely surface processes, either double layer charging/discharging or pseudocapacitive faradaic process.

Recently, Opitz et al. [50] reported that for an irreversible CV wave in absence of any capacitance current, b may be both lower and higher relative to the expected value of 0.5. The value $b = 0$ holds around the equilibrium potential, when current potential dependence is described by Butler-Volmer equation, and thus does not depend on scanning rate (i.e. $I = v^0$).

The other form of Eq. (3):

$$I = k_c v + k_d v^{1/2} \quad (4)$$

where k_c and k_d are constants (coefficients) [22,33,40,41], enables to determine separately the contribution of diffusion ($k_d v^{1/2}$) and capacitance/pseudocapacitance ($k_c v$) current in the total charge stored. According to this equation, the total current corresponding to an intercalation redox process, is the sum of diffusion (bulk) current ($k_d v^{1/2}$), which depends linearly on the square root of scan rate, and pseudocapacitance (surface) current ($k_c v$) recognizable by its linear dependence on scan rate.

In these equations, current may be either peak current, or alternatively current at a fixed potential (called isopotential testing).

One should have in mind that equations (3) and (4)) are based on assumption that migration current is eliminated, i.e. only charge transfer and mass transfer may determine the form of I-E dependence. Since this assumption is unreal in intercalation reactions, particularly if phase transition accompanies the electrochemical process, we performed the testing of the validity of equations (3) and (4) in the case of SG and SS samples.

Firstly, we calculated the average slope (b-value) of $\log I_p$ - logv plot from the cyclovoltammogams of the investigated samples, where Ip is peak current and v is the scan rate. The scan rates 5–400 mV s^{-1} were considered. This dependence is roughly linear for both samples, as Fig. 8 shows, in the complete range of scan rates.

The average b-values, calculated for the main current redox peaks of SG sample amounted to 0.65 (anodic scan) and 0.70 (cathodic scan), while the corresponding b-values of SS sample were 0.63 (anodic scan) and 0.7 (cathodic scan). It indicates that the kinetics of $LiFePO_4 \leftrightarrow FePO_4$ redox reaction is nearly diffusion controlled, as has already shown elsewhere [17,38]. The absence of the case $b = 0.5$ could mean a permanent participation of surface-controlled processes (extrinsic pseudocapacitance that differs from the intrinsic one [61]) in the total charge storage.

Equation (3) was then checked in the isopotential regime, i.e. the b-values were calculated at various fixed potentials. The isopotential regime implies the determination of the dependence of current (I) versus scan rate at a fixed potential, upon recording a set of cyclovoltammograms at various scan rates. In this regime, the discrete potentials are selected uniformly along the whole potential region of cyclic voltammetry, irrespective of the position of CV maxima. The b-values of SG sample (Fig. 9a) indicated almost pure diffusion behaviour ($b \approx 0.5$) only at the potentials corresponding nearly to the half-heights of ascending parts of both cathodic and anodic peaks (i.e, in the proximity of reversible potential). The role of pseudocapacitance increases (b tends to become equal to 1) and becomes dominant if the potential shifts toward vertex potential values. A similar trend holds in the SS case, too (Fig. 9b).

In the next step, we analyzed the available potentiodynamic data by means of equation (4) [22,40,41], which enables to determine separately the contribution of diffusion and

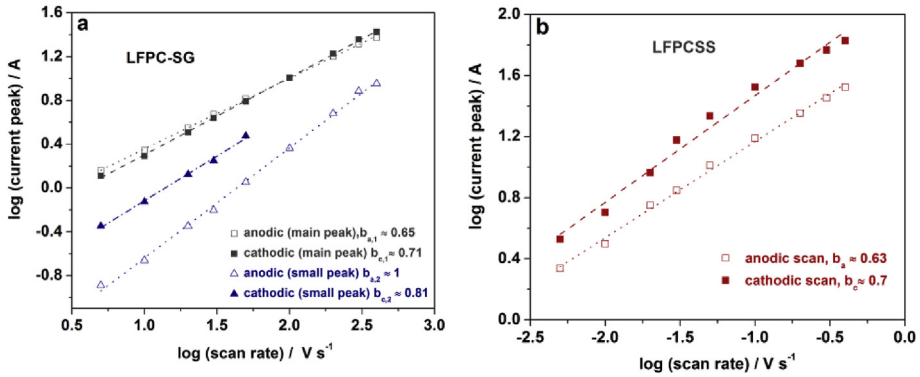

Fig. 8. log Ip - log v plot of LFPC-SG (a) and LFPC-SS whose values correspond to the main maximums of CV peaks. Their slopes against log(scan rate) axis (b values) are marked in insets.

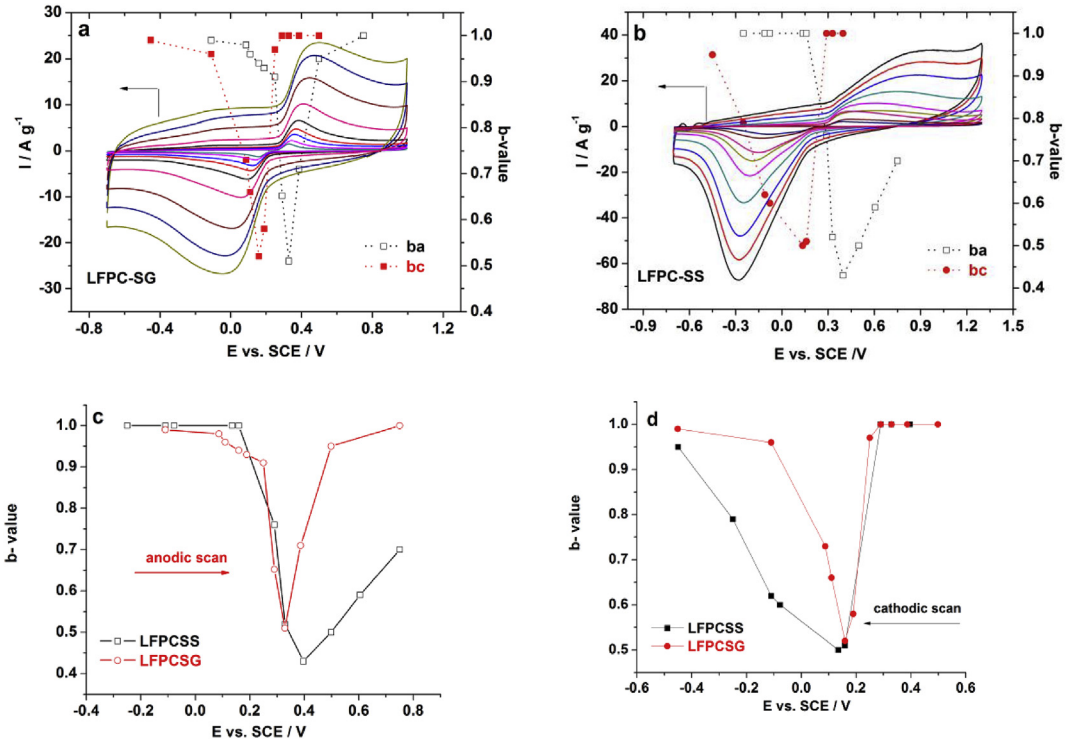

Fig. 9. b-values calculated at various potentials corresponding to the lithiation/delithiation of SG (a) and SS(b) samples. The b-values for both composites were shown in a comparative way in the insets c) and d), for the anodic and cathodic scan, respectively.

pseudocapacitance current in the total charge stored, expressed in the form more simple for practical use:

$$I/v^{1/2} = k_c v^{1/2} + k_d \quad (5)$$

This equation is used in a relatively narrow range of scan rates in Ref. [53].

Equation (5), assumes that the plot of $I/v^{1/2}$ versus $v^{1/2}$ is linear, in which k_d is the intercept on the ordinate, and k_c is the slope. When the current was peak one, its dependence on the square root of scan rate is presented in Fig. 10. Apparently, some critical value of scan rate separates two kinetic regions, shadowed by different colours. For SG sample, critical scan rate is ~200 mV s^{-1} while for SS sample, this value amounts to ~50 mV s^{-1}.

Fig. 10 shows, that contrary to expectations of straight lines based on classic CV, equation (4) is not applicable in a broad range of scanning rates. Namely, the pairs of values k_c and k_d calculated for low scan rates do not hold at high ones. Further to this, in the region of high scan rates, the slope of the graph is null, which would mean that only diffusion current is present, contrary to the general experience that capacitance current increases faster than diffusion one when scanning rate increases.

In the last step, we tested the applicability of Eq. (5) in the isopotential regime. Several potentials left, around and right relative to the equilibrium potential, was selected to construct plots $Iv'^{1/2}$ vs $v^{1/2}$. The results are presented in Fig. 11. On the basis of classic CV theory, straight lines are expected in a complete range of scanning rates. However, linear dependence was observed only in the potential regions where monophase processes took place, for example, for anodic curves at the potentials left from reversible one, and for cathodic currents at the potentials right from reversible one. Namely, in these cases, monophase Li concentration

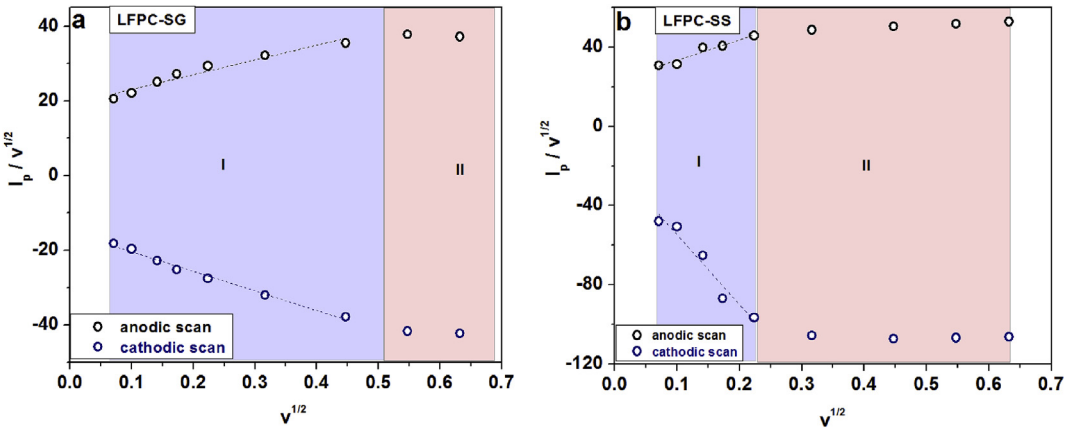

Fig. 10. The dependence of $I_p/v^{1/2}$ on $v^{1/2}$ for SG (a) and SS(b) samples. The label v refers to the scan rate.

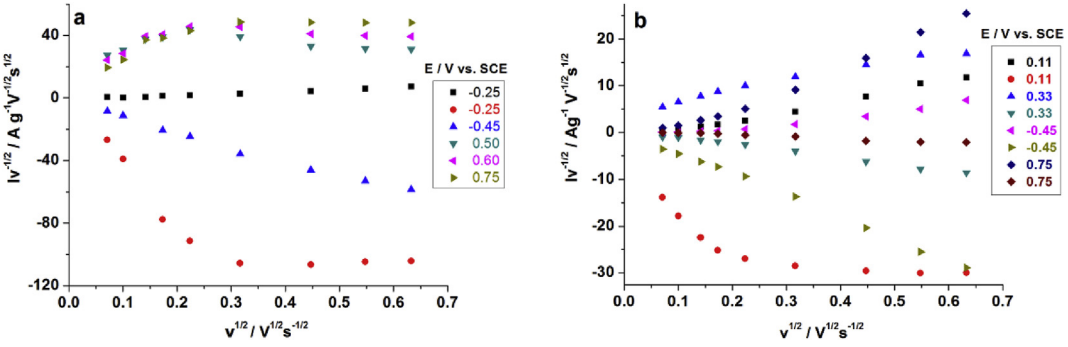

Fig. 11. The isopotential dependence of $I/v^{1/2}$ on $v^{1/2}$ for SS (left) and SG(right) samples. The potentials, both lower and higher than reversible one were used to construct graphs. The potentials for each graph are marked in insets.

depletion in $LiFePO_4$, and monophase Li concentration saturation in $FePO_4$ occur, respectively. Linear curves generally made zero intercept on the ordinate, indicating that apparently monophase processes are exclusively capacitive in nature. In the regime of phase transition, the dependence $Iv^{-1/2}$ vs $v^{1/2}$ is nonlinear, likely to that found for peak currents in Fig. 10, which may lead to an irregular correlation between diffusion and capacitance current.

This can be called experimental artifact of the iso-potential CV analysis [57] which points out the impropriety of using equation (4) in the intercalation systems with phase change. This conclusion retroactively makes the conclusions derived from Fig. 9 doubtful. The first attempt to accommodate the theory of CV to intercalation accompanied by phase transition was described by Zhu et al. [62].

Observing Figs. 5 and 6, we suggest as most likely that, at least around the reversible potential, ohmic resistance determines the kinetics of intercalation/deintercalation processes. For such a case, Dahn et al. [55], derived that the peak current depends linearly on the square root of scanning rate, while the current increases linearly with potential, thus the slope of the peak front is independent on scanning rate:

$$I_p = \left(\frac{2Q}{R}\right)^{1/2} v^{1/2} \tag{6}$$

where Q is coulombic capacity and R is polarization resistance.

Peak to peak distance for processes limited only by ohmic resistance R of the system is proportional to the square root of coulombic capacity Q, i.e.:

$$\Delta E = 2(2RQ)^{1/2} v^{1/2} \tag{7}$$

This is a very probable explanation of Fig. 7, i.e., the different peak-to-peak potential distance of samples investigated is not due to the difference in irreversibility, but due to the difference in coulombic capacities, i.e. material utilization. Namely, overlapping of CV curves of SS and SG sample for different scan rates in the proximity of reversible potential excludes any assumption on the difference in reversibility of electrochemical reactions in the samples.

To check the assumption of the applicability of Eq. (7) in the observed systems, the polarization resistance was determined in the proximity of reversible potential at slow scan rates, and the values 0.06 and 0.018 Ω g were found for SS an SG sample, respectively. For these polarization resistances, using coulombic capacitances from Fig. 7, peak-to-peak potential distances were calculated, and presented together with the experimental values in Fig. 12. The agreement is generally fair, however, since Eq. (5) does not account with the capacitance current, one should have in mind that its contribution may cause disagreements between calculated and experimental values commensurable to the scan rate.

4. Conclusions

Crystalline olivine $LiFePO_4$ phase, in the form of a composite with carbon, was synthesized by sol-gel (SG) and solid-state procedure (SS), for the sake of comparative analysis. The difference in applied synthesis procedure causes the difference in morphological and electrochemical properties of olivine.

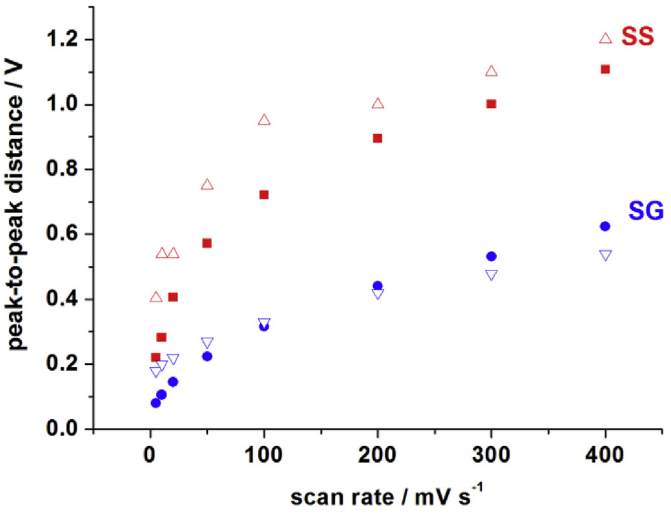

Fig. 12. Peak–to-peak potential distance in function on scan rate for SS and SG samples, experimental points (empty symbols) versus those calculated by means of Eq. (5) (full symbols).

Both composites showed the capability of lithium intercalating/deintercalating in an aqueous solution of $LiNO_3$, storing a different amount of charge. At lower scan rates, three times larger lithium storage capacity was measured for the SS sample. It reaches a high value of 74 mAh g^{-1} at 5 mV s^{-1}, while the corresponding value for sol-gel prepared sample amounted to 23 mAh g^{-1}. Conversely, SS showed a much higher capacity decrease with the scan rate increase, than SG sample. The samples lie in different regions of sensitivity of coulombic capacitance toward scanning rate, SS sample displaying higher sensitivity.

The ways to separate diffusion and capacitance current in overall stored charge, described in the literature based on classical theory of CV, were tested and have been shown to be inappropriate in this case. We suggest that the intercalation kinetics is best modelled by an ohmic resistance of the system.

Acknowledgements

The research was supported by Ministry of Education, Science and Technological Development of the Republic of Serbia through the Projects III 45014 as well as through the Projects III45004, III45015, III45019 and bilateral project Serbia- Slovenia entitled “Developments of novel materials for alkaline-ion batteries”. The Serbian Academy of Sciences and Arts supported this investigation, too, through the project “Electrocatalysis in the contemporary process of energy conversion”. The authors would like to thank Dr. Biljana Šljukić Paunković from the Faculty of Physical Chemistry, University of Belgrade for SEM measurements.

Appendix A. Supplementary data

Supplementary data to this article can be found online at https://doi.org/10.1016/j.jallcom.2018.10.246.

References

[1] A.K. Padhi, K.S. Nanjunclaswamy, C. Masquelier, S. Okada, Effect of structure on the Fe^{3+}/Fe^{2+} redox couple in iron phosphates, J. Electrochem. Soc. 144 (1997) 1609–1613.
[2] B. Kang, G. Ceder, Battery materials for ultrafast charging and discharging, Nature 458 (2009) 190–193, https://doi.org/10.1038/nature07853.
[3] S.Y. Chung, J.T. Bloking, Y.M. Chiang, Electronically conductive phospho-olivines as lithium storage electrodes, Nat. Mater. 1 (2002) 123–128, https://doi.org/10.1038/nmat732.
[4] M.S. Islam, D.J. Driscoll, C.A.J. Fisher, P.R. Slater, Atomic-scale investigation of defects, dopants, and lithium transport in the $LiFePO_4$ olivine-type battery material, Chem. Mater. 17 (2005) 5085–5092, https://doi.org/10.1021/cm050999v.
[5] S.F. Yang, P.Y. Zavalij, M.S. Whittingham, Hydrothermal synthesis of lithium iron phosphate cathodes, Electrochem. Commun. 3 (2001) 505–508, https://doi.org/10.1016/S1388-2481(01)00200-4.
[6] Y. Wang, Y. Wang, E. Hosono, K. Wang, H. Zhou, The design of a $LiFePO_4$/carbon nanocomposite with a core-shell structure and its synthesis by an in situ polymerization restriction method, Angew. Chem. Int. Ed. 47 (2008) 7461–7465, https://doi.org/10.1002/anie.200802539.
[7] K. Naoi, K. Kisu, E. Iwama, S. Nakashima, Y. Sakai, Y. Orikasa, P. Leone, N. Dupré, T. Brousse, P. Rozier, W. Naoi, P. Simon, Ultrafast charge–discharge characteristics of a nanosized core–shell structured $LiFePO_4$ material for hybrid supercapacitor applications, Energy Environ. Sci. 9 (2016) 2143–2151, https://doi.org/10.1039/C6EE00829A.
[8] W.L. Liu, J.P. Tu, Y.Q. Qiao, J.P. Zhou, S.J. Shi, X.L. Wang, C.D. Gu, Optimized performances of core-shell structured $LiFePO_4$/C nanocomposite, J. Power Sources 196 (2011) 7728–7735, https://doi.org/10.1016/j.jpowsour.2011.05.046.
[9] M. Manickam, P. Singh, S. Thurgate, K. Prince, Redox behavior and surface characterization of $LiFePO_4$ in lithium hydroxide electrolyte, J. Power Sources 158 (2006) 646–649, https://doi.org/10.1016/j.jpowsour.2005.08.059.
[10] M. Vujković, D. Jugović, M. Mitrić, I. Stojković, N. Cvjetićanin, S. Mentus, The $LiFe_{(1-x)}V_xPO_4$/C composite synthesized by gel-combustion method, with improved rate capability and cycle life in aerated aqueous solutions, Electrochim. Acta 109 (2013) 835–842, https://doi.org/10.1016/j.electacta.2013.07.219.
[11] M. Vujković, I. Stojković, N. Cvjetićanin, S. Mentus, Gel-combustion synthesis of $LiFePO_4$/C composite with improved capacity retention in aerated aqueous electrolyte solution, Electrochim. Acta 92 (2013) 248–256, https://doi.org/10.1016/j.electacta.2013.01.030.
[12] Y. Zhu, Y. Xu, Y. Liu, C. Luo, C. Wang, Comparison of electrochemical performances of olivine $NaFePO_4$ in sodium-ion batteries and olivine $LiFePO_4$ in lithium-ion batteries, Nanoscale 5 (2013) 780–787, https://doi.org/10.1039/C2NR32758A.
[13] N. Alias, A.A. Mohamad, Synthesis and electrochemical behavior of $LiFePO_4$/C with an air-electrode in an aqueous lithium ion battery, Ceram. Int. 40 (2014) 13089–13096, https://doi.org/10.1016/j.ceramint.2014.05.008.
[14] A. Tron, Y.N. Jo, S.H. Oh, Y.D. Park, J. Mun, Surface modification of the $LiFePO_4$ cathode for the aqueous rechargeable lithium ion battery, ACS Appl. Mater. Interfaces 9 (2017) 12391–12399, https://doi.org/10.1021/acsami.6b16675.
[15] J.Y. Luo, W.J. Cui, P. He, Y.Y. Xia, Raising the cycling stability of aqueous lithium-ion batteries by eliminating oxygen in the electrolyte, Nat. Chem. 2 (2010) 760–765, https://doi.org/10.1038/nchem.763.
[16] N. Alias, A.A. Mohamad, Advances of aqueous rechargeable lithium-ion battery: a review, J. Power Sources 274 (2015) 237–251, https://doi.org/10.1016/j.jpowsour.2014.10.009.
[17] P. Simon, Y. Gogotsi, B. Dunn, Where do batteries end and supercapacitors begin? Science 343 (2014) 1210–1211, https://doi.org/10.1126/science.1249625.
[18] T. Brousse, D. Belanger, J.W. Long, To Be or not to Be pseudocapacitive? J. Electrochem. Soc. 162 (2015) A5185–A5189, https://doi.org/10.1149/2.0201505jes.
[19] P.G. Bruce, B. Scrosati, J.-M. Tarascon, Nanomaterials for rechargeable lithium batteries, Angew. Chem. Int. Ed. 47 (2008) 2930–2946, https://doi.org/10.1002/anie.200702505.
[20] A. Mahmoud, J.M. Amarilla, K. Lasri, I. Saadoune, Influence of the synthesis method on the electrochemical properties of the $Li_4Ti_5O_{12}$ spinel in Li-half and Li-ion full-cells. A systematic comparison, Electrochim. Acta 93 (2013) 163–172, https://doi.org/10.1016/j.electacta.2013.01.083.
[21] Y. Xia, M. Yoshio, H. Noguchi, Improved electrochemical performance of $LiFePO_4$ by increasing its specific surface area, Electrochim.Acta 52 (2006) 240–245, https://doi.org/10.1016/j.electacta.2006.05.002.
[22] V. Augustyn, J. Come, M.A. Lowe, J.W. Kim, P.L. Taberna, S.H. Tolbert, H.D. Abruña, P. Simon, B. Dunn, High-rate electrochemical energy storage through Li^+ intercalation pseudocapacitance, Nat. Mater. 26 (2016) 7263–7270, https://doi.org/10.1038/nmat3601.
[23] S. Lou, X. Cheng, L. Wang, J. Gao, Q. Li, Y. Ma, Y. Gao, P. Zuo, C. Du, H. Huo, G. Yin, High-rate capability of three-dimensionally ordered macroporous T-Nb_2O_5 through Li^+ intercalation pseudocapacitance, J. Power Sources 361 (2017) 80–86, https://doi.org/10.1016/j.jpowsour.2017.06.023.
[24] S. Lou, X. Cheng, J. Gao, Q. Li, L. Wang, Y. Cao, Y. Ma, P. Zuo, Y. Gao, C. Du, H. Huo, G. Yin, Pseudocapacitive Li^+ intercalation in porous $Ti_2Nb_{10}O_{29}$ nanospheres enables ultra-fast lithium storage, Energy Storage Mater. 11 (2018) 57–66, https://doi.org/10.1016/j.ensm.2017.09.012.
[25] M. Lübke, N. Ding, M.J. Powell, D.J.L. Brett, P.R. Shearing, Z. Liu, J.A. Darr, VO_2 nano-sheet negative electrodes for lithium-ion batteries, Electrochem. Commun. 64 (2016) 56–60, https://doi.org/10.1016/j.elecom.2016.01.013.
[26] M. Lübke, P. Marchand, D.J.L. Brett, P. Shearing, R. Gruar, Z. Liu, J.A. Darr, High power layered titanate nano-sheets as pseudocapacitive lithium-ion battery anodes, J. Power Sources 305 (2016) 115–121, https://doi.org/10.1016/j.jpowsour.2015.11.060.
[27] R. Sun, Q. Wei, J. Sheng, C. Shi, Q. An, S. Liu, L. Mai, Novel layer-by-layer

stacked VS_2 nanosheets with intercalation pseudocapacitance for high-rate sodium ion charge storage, Nano Energy 35 (2017) 396–404, https://doi.org/10.1016/j.nanoen.2017.03.036.
[28] A. Eftekhari, M. Mohamedi, Tailoring pseudocapacitive materials from a mechanistic perspective, Mater. Today Energy 6 (2017) 211–229, https://doi.org/10.1016/j.mtener.2017.10.009.
[29] G.A. Muller, J.B. Cook, H.S. Kim, S.H. Tolbert, B. Dunn, High performance pseudocapacitor based on 2D layered metal chalcogenide nanocrystals, Nano Lett. 15 (2015) 1911–1917, https://doi.org/10.1021/nl504764m.
[30] J.B. Cook, H.S. Kim, T.C. Lin, C.H. Lai, B. Dunn, S.H. Tolbert, Pseudocapacitive charge storage in thick composite MoS_2 nanocrystal-based electrodes, Adv. Energy Mater. 7 (2016) 1–12, https://doi.org/10.1002/aenm.201601283.
[31] T. Brezesinski, J. Wang, S.H. Tolbert, B. Dunn, Ordered mesoporous α-MoO_3 with iso-oriented nanocrystalline walls for thin-film pseudocapacitors, Nat. Mater. 9 (2010) 146–151, https://doi.org/10.1038/nmat2612.
[32] J. Wu, Z. Lu, K. Li, J. Cui, S. Yao, M. Ihsan-ul Haq, B. Li, Q.-H. Yang, F. Kang, F. Ciucci, J.-K. Kim, Hierarchical MoS_2/carbon microspheres as long-life and high-rate anodes for sodium-ion batteries, J. Mater. Chem. A. 0 (2018) 1–10, https://doi.org/10.1039/C7TA11119C.
[33] J. Wan, X. Yao, X. Gao, X. Xiao, T. Li, J. Wu, W. Sun, Z. Hu, H. Zu, L. Huang, M. Liu, J. Zhou, Microwave combustion for modification of transition metal oxides, Adv. Funct. Mater. 26 (2016) 7263–7270, https://doi.org/10.1002/adfm.201603125.
[34] J. Wu, X. Gao, H. Yu, T. Ding, Y. Yan, B. Yao, X. Yao, D. Chen, M. Liu, L. Huang, A scalable free-standing V_2O_5/CNT film electrode for supercapacitors with a wide operation voltage (1. 6 V) in an aqueous electrolyte, Adv. Funct. Mater. 26 (2016) 6114–6120, https://doi.org/10.1002/adfm.201601811.
[35] L. Huang, B. Yao, J. Sun, X. Gao, J. Wu, J. Wan, T. Li, Z. Hu, J. Zhou, Highly conductive and flexible molybdenum oxide nanopaper for high volumetric supercapacitor, J. Mater. Chem. A 5 (2017) 2897–2903, https://doi.org/10.1039/c6ta10433a.
[36] M. Vujković, S. Mentus, Potentiodynamic and galvanostatic testing of $NaFe_{0.95}V_{0.05}PO_4$/C composite in aqueous $NaNO_3$ solution, and the properties of aqueous $Na_{1.2}V_3O_8$/$NaNO_3$/$NaFe_{0.95}V_{0.05}PO_4$/C battery, J. Power Sources 325 (2016) 185–193, https://doi.org/10.1016/j.jpowsour.2016.06.031.
[37] P. Yu, C. Li, X. Guo, Sodium storage and pseudocapacitive charge in textured $Li_4Ti_5O_{12}$ thin films, J. Phys. Chem. C 118 (2014) 10616–10624, https://doi.org/10.1021/jp5010693.
[38] J. Come, P.-L. Taberna, S. Hamelet, C. Masquelier, P. Simon, Electrochemical kinetic study of $LiFePO_4$ using cavity microelectrode, J. Electrochem. Soc. 158 (2011) A1090, https://doi.org/10.1149/1.3619791.
[39] Y. Wang, D. Zhao, R. Che, Y. Xia, Pseudo-capacitive profile vs. Li-intercalation in Nano-$LiFePO_4$, J. Power Sources 236 (2013) 230–237, https://doi.org/10.1016/j.jpowsour.2013.02.071.
[40] V. Augustyn, P. Simon, B. Dunn, Pseudocapacitive oxide materials for high-rate electrochemical energy storage, Energy Environ. Sci. 7 (2014) 1597, https://doi.org/10.1039/c3ee44164d.
[41] J. Wang, J. Polleux, J. Lim, B. Dunn, Pseudocapacitive contributions to electrochemical energy storage in TiO_2 (anatase) nanoparticles, J. Phys. Chem. C 111 (2007) 14925–14931, https://doi.org/10.1021/jp074464w.
[42] R. Li, J. Liu, Mechanistic investigation of the charge storage process of pseudocapacitive Fe_3O_4 nanorod film, Electrochim. Acta 120 (2014) 52–56, https://doi.org/10.1016/j.electacta.2013.12.040.
[43] M. Lübke, A. Sumboja, I.D. Johnson, D.J.L. Brett, P.R. Shearing, Z. Liu, J.A. Darr, High power nano-Nb_2O_5 negative electrodes for lithium-ion batteries, Electrochim. Acta 192 (2016) 363–369, https://doi.org/10.1016/j.electacta.2016.01.226.
[44] M. Lübke, J. Shin, P. Marchand, D. Brett, P. Shearing, Z. Liu, J.A. Darr, Highly pseudocapacitive Nb-doped TiO_2 high power anodes for lithium-ion batteries, J. Mater. Chem. A. 3 (2015) 22908–22914, https://doi.org/10.1039/C5TA07554H.
[45] D.Y.W. Yu, C. Fietzek, W. Weydanz, K. Donoue, T. Inoue, H. Kurokawa, S. Fujitani, Study of LiFePO[sub 4] by cyclic voltammetry, J. Electrochem. Soc. 154 (2007) A253, https://doi.org/10.1149/1.2434687.
[46] H. Matsui, T. Nakamura, Y. Kobayashi, M. Tabuchi, Y. Yamada, Open-circuit voltage study on $LiFePO_4$ olivine cathode, J. Power Sources 195 (2010) 6879–6883, https://doi.org/10.1016/j.jpowsour.2010.04.072.
[47] K. Kisu, E. Iwama, W. Naoi, P. Simon, K. Naoi, Electrochemical kinetics of nanostructure $LiFePO_4$/graphitic carbon electrodes, Electrochem. Commun. 72 (2016) 10–14, https://doi.org/10.1016/j.elecom.2016.08.013.
[48] F. Sauvage, L. Laffont, J.M. Tarascon, E. Baudrin, Factors affecting the electrochemical reactivity vs. lithium of carbon-free $LiFePO_4$ thin films, J. Power Sources 175 (2008) 495–501, https://doi.org/10.1016/j.jpowsour.2007.09.085.
[49] D. Panias, M. Taxiarchou, I. Douni, I. Paspaliaris, A. Kontopoulos, Thermodynamic analysis of the reactions of iron Oxides: dissolutiona in oxalic acid, Can. Metall. Q. 35 (1996) 363–373, https://doi.org/10.1179/cmq.1996.35.4.363.
[50] A. Le Bail, H. Duroy, J.L. Fourquet, Ab-initio structure determination of $LiSbWO_6$ by X-ray powder diffraction, Mater. Res. Bull. 23 (1988) 447–452.
[51] R.W. Cheary, A. Coelho, A fundamental parameters approach to X-ray line-profile fitting, J. Appl. Crystallogr. 25 (1992) 109–121, https://doi.org/10.1107/S0021889891010804.
[52] I. Belharouak, C. Johnson, K. Amine, Synthesis and electrochemical analysis of vapor-deposited carbon-coated LiFePO4, Electrochem. Commun. 7 (2005) 983–988, https://doi.org/10.1016/j.elecom.2005.06.019.
[53] R. Dominko, M. Bele, M. Gaberscek, M. Remskar, D. Hanzel, S. Pejovnik, J. Jamnik, Impact of the carbon coating thickness on the electrochemical performance of $LiFePO_4$/C composites, J. Electrochem. Soc. 152 (2005) A607, https://doi.org/10.1149/1.1860492.
[54] R. Dominko, M. Bele, M. Gaberscek, M. Remskar, D. Hanzel, J.M. Goupil, S. Pejovnik, J. Jamnik, Porous olivine composites synthesized by sol-gel technique, J. Power Sources 153 (2006) 274–280, https://doi.org/10.1016/j.jpowsour.2005.05.033.
[55] J.R. Dahn, R.R. Haering, The role of kinetic effects in voltammetry studies of intercalation systems, Solid State Ionics 2 (1981) 19–26, https://doi.org/10.1016/0167-2738(81)90014-X.
[56] M. Vujković, M. Mitrić, S. Mentus, High-rate intercalation capability of $NaTi_2(PO_4)_3$/C composite in aqueous lithium and sodium nitrate solutions, J. Power Sources 288 (2015) 176–186, https://doi.org/10.1016/j.jpowsour.2015.04.132.
[57] M. Opitz, J. Yue, J. Wallauer, B. Smarsly, B. Roling, Mechanisms of charge storage in nanoparticulate TiO_2 and $Li_4Ti_5O_{12}$ anodes: new insights from scan rate-dependent cyclic voltammetry, Electrochim. Acta 168 (2015) 125–132, https://doi.org/10.1016/j.electacta.2015.03.186.
[58] M. Sathiya, A.S. Prakash, K. Ramesha, J. Tarascon, A.K. Shukla, V 2 O 5 -anchored carbon nanotubes for enhanced electrochemical energy storage, J. Am. Chem. Soc. 133 (2011) 16291–16299, https://doi.org/10.1021/ja207285b.
[59] H. Lindström, S. Södergren, A. Solbrand, H. Rensmo, J. Hjelm, A. Hagfeldt, S.-E. Lindquist, Li^+ ion insertion in TiO $_2$ (anatase). 2. Voltammetry on nanoporous films, J. Phys. Chem. B 101 (1997) 7717–7722, https://doi.org/10.1021/jp970490q.
[60] K. Zhu, Q. Wang, J.H. Kim, A.A. Pesaran, A.J. Frank, Pseudocapacitive lithium-ion storage in oriented anatase TiO2nanotube arrays, J. Phys. Chem. C 116 (2012) 11895–11899, https://doi.org/10.1021/jp301884x.
[61] L. Huang, X. Yao, L. Yuan, B. Yao, X. Gao, J. Wan, P. Zhou, M. Xu, J. Wu, H. Yu, Z. Hu, T. Li, Y. Li, J. Zhou, 4-Butylbenzenesulfonate modified polypyrrole paper for supercapacitor with exceptional cycling stability, Energy Storage Mater. 12 (2018) 191–196, https://doi.org/10.1016/j.ensm.2017.12.016.
[62] Y. Zhu, C. Wang, Novel CV for phase transformation electrodes, J. Phys. Chem. C 115 (2011) 823–832, https://doi.org/10.1021/jp109954y.